Mathematical Modeling and Algorithm Application
ISSN: 3006-0842 | Vol. 8, No. 1, 2026

Spallation Behavior of Cu-Ni Nanowires Under Shock Loading

Jierui Jiang[1,*], Yi Liao[1], Xiao Zhou[1], Tao Wen[2]

[1]School of Mechanical Engineering, Southwest Petroleum University, Chengdu, 610500, China

[2]Well Testing Company, Western Drilling Engineering Company Limited, China National Petroleum Corporation, Karamay City, 834000, China

[*] **Corresponding author**: Jierui Jiang (Email: 935137192@qq.com)

Abstract: In the study of the dynamic evolution of Cu-Ni FGM NWs models, for the three functions P-FGM, E-FGM, and S-FGM, the trends of their density, temperature, velocity, and stress dynamic evolution are consistent. Throughout the impact loading process, the sample experiences a compression stage, followed by a stretching stage where the deformation gradually recovers. Finally, the tensile stress causes the sample to enter the spallation stage. In the study of the impact of the function parameter p on the model, for the P-FGM and E-FGM functions, the increase in p (the proportion of copper in the sample) leads to the formation of a denser compression zone under the impact wave, an increase in the number of voids, and a decrease in spalling strength and free surface velocity. In the S-FGM function, as p increases, under the impact loading, the model has higher density in the compression region, more voids, and lower spalling strength. At this point, the distribution of Cu dominates the influence on the sample.

Keywords: Graded Materials; Spallation; Shock Wave; Damage evolution.

1. Introduction

Advanced components in fields such as aerospace, automotive manufacturing, microelectronic systems, structural engineering, and biomedicine often demand performance that exceeds the boundaries of conventional engineering materials. When parts must operate in high-temperature, high-pressure environments while simultaneously possessing mechanical strength and chemical inertness—such as aero-engine turbine blades, high-temperature automotive sensors, or implantable artificial joints—traditional material systems often face the bottleneck of mutually exclusive properties. To address this, a synergistic optimization of material composition and microstructural topology is essential, enabling the component to achieve a unified adaptation of these contradictory attributes at a functional level. Consequently, Functionally Graded Materials (FGMs) are widely used around the world as cutting-edge materials. They are composed of two or more different materials, with their composition continuously varying along a dimension tailored for a specific function[1]. FGMs are primarily employed to address issues such as high stress concentration, high-temperature creep, and material delamination[2]. This also makes FGMs candidate materials for manufacturing aircraft structures, automotive engine components, and protective coatings for turbine blades[3].

In recent years, due to the applications of FGMs in aerospace, automotive, pharmaceutical, and energy fields[4], research on characterizing their mechanical and thermal properties has grown rapidly. The properties of FGMs can be altered according to various applications. N. Noda proposed a new category of composite materials, namely Functionally Graded Materials (FGMs)[5], based on observations of naturally evolved materials and structures (such as wood cross-sections, bones, teeth, and fish bodies[6][8]), which are composed of gradient structures and exhibit anisotropy when measured in different directions[9][10]. Fei Chen et al.[11]studied the influence of the microstructure on the mechanical properties of AlN/Mo functionally graded materials. Indentation and bending tests were conducted on FGMs with different composition exponent p-values. The results showed that the distribution of the two components is the most critical factor in improving bending strength and shear strength. Wagih et al.[12]investigated the contact problem between an elastoplastic functionally graded substrate and a rigid spherical indenter using the finite element method. The results indicated that the indentation responses of elastic, elastoplastic, and perfectly elastoplastic FGMs are significantly influenced by the distribution of material properties. The application of FGMs has shifted towards complex micro/nano-scale electronic and energy conversion devices, such as broadband ultrasonic transducers, solid oxide fuel cells [13], and high-current connectors[14]. Shuai Ma et al.[15] conducted research on functionally graded material electrodes. Their study demonstrated that FGM electrodes can significantly reduce interfacial stress and alleviate local stress concentration. Vasavi Boggarapu et al.[16]developed a five-layer aluminum-copper metallic FGM, finding that erosion wear decreases as the copper content increases. Li et al.[17] performed tensile loading on Au-Ag alloys, and the results indicated that the distribution function parameters play a crucial regulatory role in the mechanical properties (elastic modulus and ultimate tensile strength) of FGMs. Zhou et al.[18]employed molecular dynamics simulations to study the tribological properties and deformation mechanisms of Cu-Ni alloys at the nanoscale, particularly the effects of temperature, sliding speed, and alloy composition on frictional performance and deformation modes. The research showed that the frictional force, wear, and deformation behavior of Cu-Ni alloys at the nanoscale are significantly different from those at the macroscopic scale. Under conditions of increasing sliding speed and temperature, the friction coefficient and wear rate of the material change, with high temperature and high-speed friction exacerbating

surface plastic deformation. Furthermore, the article analyzed the effect of different copper-to-nickel ratios in Cu-Ni alloys on frictional performance, finding that alloy composition and microstructure have a significant impact on frictional behavior at the nanoscale. Fang et al. [19] used molecular dynamics simulations to study the mechanical behavior and surface deformation mechanisms of Cu-Ni alloys during nanoimprinting, focusing on the effects of imprinting force, imprinting speed, and alloy composition on surface deformation. The study revealed that higher imprinting force and speed promote more plastic deformation and the formation of local dislocations. Meanwhile, the composition ratio of Cu-Ni alloys plays a decisive role in the material's hardness, toughness, and deformation characteristics. Higher copper content leads to better plasticity, while increased nickel content improves resistance to deformation. Relying on continuum mechanics and the Finite Element Method (FEM)[25], extensive research has been conducted to understand the mechanical properties of FGMs. The von Kármán theory has been applied to large deformations to obtain analytical solutions for FGM plates under transverse mechanical loads[24]. By using the Variational Asymptotic Method (VAM)[25], analytical expressions for closed-form FGM cylinders were established. The nonlinear thermoelasticity of functionally graded ceramic-metal plates was described, taking into account transverse shear strain and rotational inertia[26]. The finite element method was used to study the mechanical behavior of functionally graded nanoscale cylinders under radial pressure, showing that material inhomogeneity has a significant influence on radial and circumferential stresses[27]. All the aforementioned studies on FGM properties are based on theoretical models or FEM associated with classical mechanics approaches.

To meet the diverse engineering application needs of functionally graded material (FGM) nanostructures, systematic research on the multi-field coupled properties of their mechanical, thermal, and electronic characteristics at the nanoscale is essential. Within this research scope, molecular dynamics (MD) simulation, with its advantage of atomic-level resolution, has become one of the most effective methods for high-precision characterization of the mechanical behavior of materials at the nanoscale.

Nano functionally graded materials are a class of materials that possess gradually varying compositional and structural properties across different levels and scales. By optimizing the functionality of each layer at the nanoscale (such as hardness, thermal conductivity, and electrical conductivity), they are endowed with outstanding comprehensive performance. FGM materials exhibit excellent properties such as heat resistance, corrosion resistance, and wear resistance, and are capable of withstanding significant stress and temperature fluctuations under extreme environmental conditions. Consequently, FGMs are widely used in high-demand fields such as aerospace, automotive, energy, electronics, and healthcare, and are particularly suitable for high-performance applications that endure harsh operating conditions.

Molecular dynamics simulations play a crucial role in the study of impact loading on metallic materials, especially in the analysis of material responses under extreme conditions. Traditional experimental methods have certain limitations, such as short experimental timeframes, difficulty in controlling strain rates, and challenges in directly observing material behavior under high-temperature and high-pressure environments. In contrast, molecular dynamics simulations can provide a dynamic view at the atomic level, revealing microscopic deformation mechanisms of materials under high strain rates, including plastic deformation, crack propagation, spallation, and melting. Through molecular dynamics simulations, researchers can precisely track the propagation of shock waves in materials, observe dramatic local changes in temperature and pressure, and the resulting phenomena such as phase transitions and fracture. Furthermore, molecular dynamics simulations can delve into studying special phenomena that traditional experimental methods cannot achieve, for example, local melting below the equilibrium melting temperature and chemical reactions far from equilibrium states. Compared with experimental methods, molecular dynamics simulations can provide more precise results, particularly in simulating realistic dynamic processes in terms of strain rates and time scales, thereby compensating for the shortcomings of experimental observation. Thus, molecular dynamics simulations provide important theoretical support and experimental evidence for understanding the deformation mechanisms, fracture processes, and phase transition behaviors of metallic materials under strong impact loading, greatly advancing research and development in the field of materials science.

2. Simulation Methods and Modeling for Cu-Ni

Using molecular dynamics simulations, the influence of different grading functions on the mechanical properties of functionally graded materials was analyzed. The effects of functional parameters and impact velocity on the performance of functionally graded materials were investigated. We selected Cu and Ni as the alloy components for the radially graded functionally graded material. On the one hand, copper and nickel, due to their excellent physical and chemical properties, are widely used in various industrial fields, particularly in the design of nanoelectronics and alloy materials[28]. Copper is extensively employed in electronic devices, wires, cables, and electrical contacts owing to its superior electrical conductivity, thermal conductivity, and corrosion resistance. Nickel, on the other hand, offers strong corrosion resistance, high-temperature durability, and good mechanical strength, making it widely used in the manufacturing of alloys, catalysts, and high-performance battery materials. On the other hand, in Cu–Ni alloys, especially at temperatures below 1085°C, the alloy forms a single phase. In this phase, nickel atoms randomly substitute for copper atoms, occupying the lattice sites of the face-centered cubic (FCC) structure of copper. This indicates that, at lower temperatures, copper and nickel form a uniform solid solution in the lattice, maintaining a stable structure. This homogeneous mixing characteristic allows Cu–Ni alloys to exhibit excellent mechanical properties and corrosion resistance in practical applications, making them particularly suitable for high-strength, high-temperature, and corrosion-resistant environments. Furthermore, their nearly identical lattice constants (Ni: 3.52 Å, Cu: 3.60 Å) result in relatively insignificant lattice mismatch and residual strain. To construct an FGM model with a reasonably stable structure, the average lattice constant (aFGM= (aCu+ aNi)/2 = 3.56 Å) was set as the lattice constant for both Cu and Ni for simulating the impact tests. A cuboid-shaped Cu–Ni alloy was used for the impact test simulations (taking P-FGM with p = 1 as an

example), as shown in Figure 1.

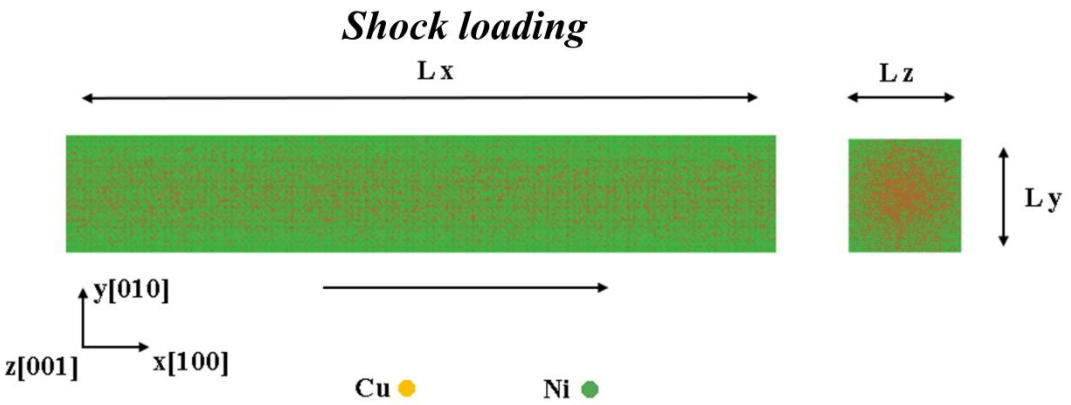


Figure 1: Model for the impact test (taking P-FGM, p = 1 as an example)

In the figure, Lx, Ly, and Lz represent the dimensions of the model along the x, y, and z directions, respectively. The parameters of the model for the impact test are listed in Table 1. It is worth noting that the table shows the total number of atoms in the model, but the individual counts of Cu and Ni atoms depend on the grading function used to construct the sample. The Cu-Ni FGM model belongs to the face-centered cubic (FCC) crystal structure, with crystal orientations along the x, y, and z directions being [100], [010], and [001], respectively. In the simulation, periodic boundary conditions are applied in the y and z directions, while free boundary conditions are used in the x direction (the loading direction).

During the simulation tests, the conjugate gradient method is first employed to minimize the energy of the Cu-Ni P-FGM model. Then, under the NPT ensemble, the model is relaxed for 25 ps at 0 GPa and 300 K to achieve a relaxed steady state. Subsequently, a "piston-block" loading method is used to generate shock waves in the sample, with shock intensities of 1.0 km/s and 2.0 km/s applied in subsequent simulations. To ensure the accuracy of the simulation results, the time step for relaxation and shock simulation is set to 0.00025 ps, with a total simulation time of 80 ps, ensuring that all models experience spallation damage within this timeframe.

Table 1 Model Dimensions and Total Number of Atoms for FGM

	Lx (nm)	Ly (nm)	Lz (nm)	Number of atoms
Impact test	142.4	17.8	17.8	4000000

The interactions between all atoms in the simulation region are described by the Embedded Atom Method (EAM) potential[29]. In this method, the EAM and its variants are widely used in the field of metals. The potential energy of atom *i*is given by the following formula:

$$E_i = F_\alpha\left(\sum_{i\neq j}\rho_\beta(r_{ij})\right) + \frac{1}{2}\sum_{i\neq j}\emptyset_{\alpha\beta}(r_{ij}) \qquad (1)$$

Here, *rij* is the distance between atoms *i*and *j*, ∅αβis a pairwise potential function, ρβrepresents the contribution of atom *j*to the electron charge density at the position of atom *i*, and Fα is an embedding function denoting the energy required to place atom *i*into the electron cloud. α and β denote the element types of atoms *i* and *j*, respectively.

The potential function selected for this simulation was fitted by Bonny et al[30]. This copper-nickel alloy potential function, based on the Embedded Atom Method (EAM), improves the accuracy and efficiency of alloy simulations through parameter optimization. This model accurately describes the interatomic interactions within Cu-Ni alloys and shows high consistency with experimental data, particularly demonstrating high accuracy in predicting the alloy's crystal structure, thermodynamic properties, and phase behavior. The EAM model significantly enhances computational efficiency during large-scale molecular dynamics simulations, making it suitable for more complex alloy design and materials research. Furthermore, this potential function exhibits good adaptability and flexibility, providing reliable results under various temperature and pressure conditions.

The Cu-Ni FGM model can be generated by continuously varying the composition ratio of the constituent materials from the inside to the outside along the radial direction. Establishing the Cu-Ni FGM model involves the following three steps: (1) Generate a single-crystal Cu model of the desired dimensions. (2) Subdivide the FGM model into several annular cylinders, each with a thickness of 1.78 Å (half of the lattice constant). (3) Within each annular cylinder, randomly replace Cu atoms with Ni atoms according to the grading function. The grading functions considered in the simulation are the power-law function[31], the sigmoid function 错误!未找到引用源。, and the exponential function[32]. The corresponding FGM models are denoted as P-FGM, S-FGM, and E-FGM, respectively. The calculation formulas are listed in Table 2.

Table 2 Ni atom fraction in FGM

Types of FGM	Grading function	Distribution of Ni in Cu, g(r)
P-FGM	Power-law function	$g(r)=\left(\frac{r}{R}\right)^{p}$
E-FGM	Exponential function	$g(r)=1-e^{-\left(\frac{r}{R}\right)^{p}}$
S-FGM	Sigmoid function	$g(r)=\frac{1}{2}\left(2\frac{r}{R}\right)^{p}$; $0\le r\le\frac{R}{2}$ $g(r)=1-\frac{1}{2}\left(2\left(1-\frac{r}{R}\right)\right)^{p}$; $\frac{R}{2}\le r\le R$

p —— Function parameters;

R —— Radial distance from the model center

By varying the function parameter *p*, FGM models with various grading profiles can be generated. Figure 2 displays the radial distribution of the mass fraction of Cu in the Cu-Ni FGM model for different *p* values. To visually represent the radial distribution of Cu and Ni atoms, Figure 3 provides cross-sectional views of the models under different *p* values.

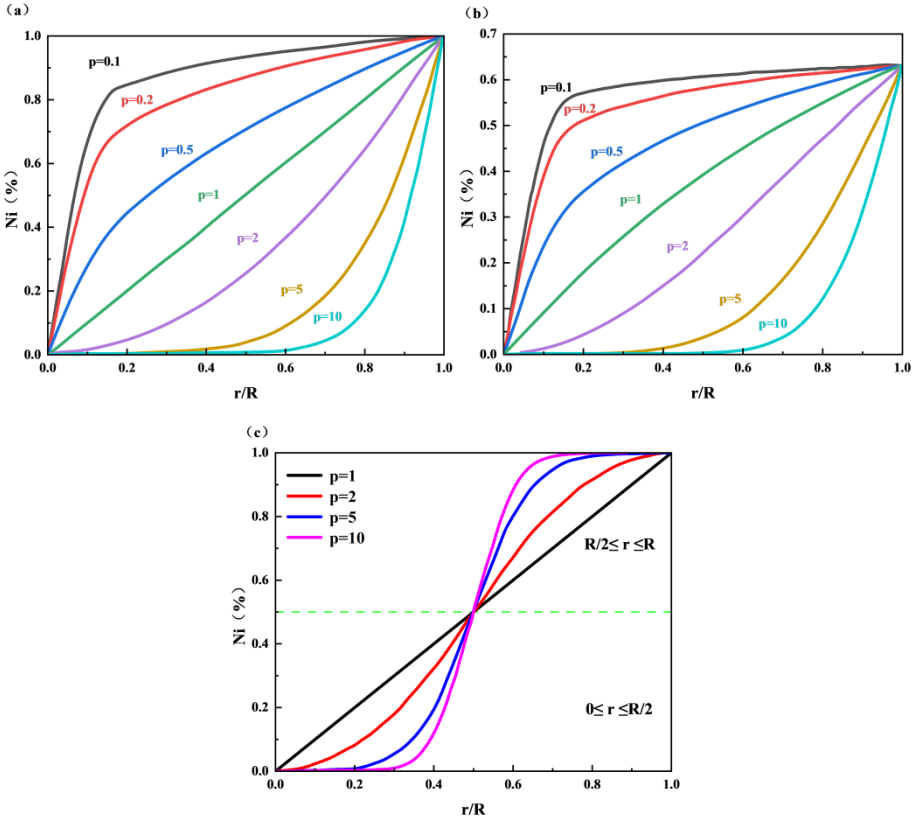


Figure 2: Radial distribution of the mass fraction of Ni in Cu under different function parameter *p* values: (a) P-FGM function; (b) E-FGM function; (c) S-FGM function.

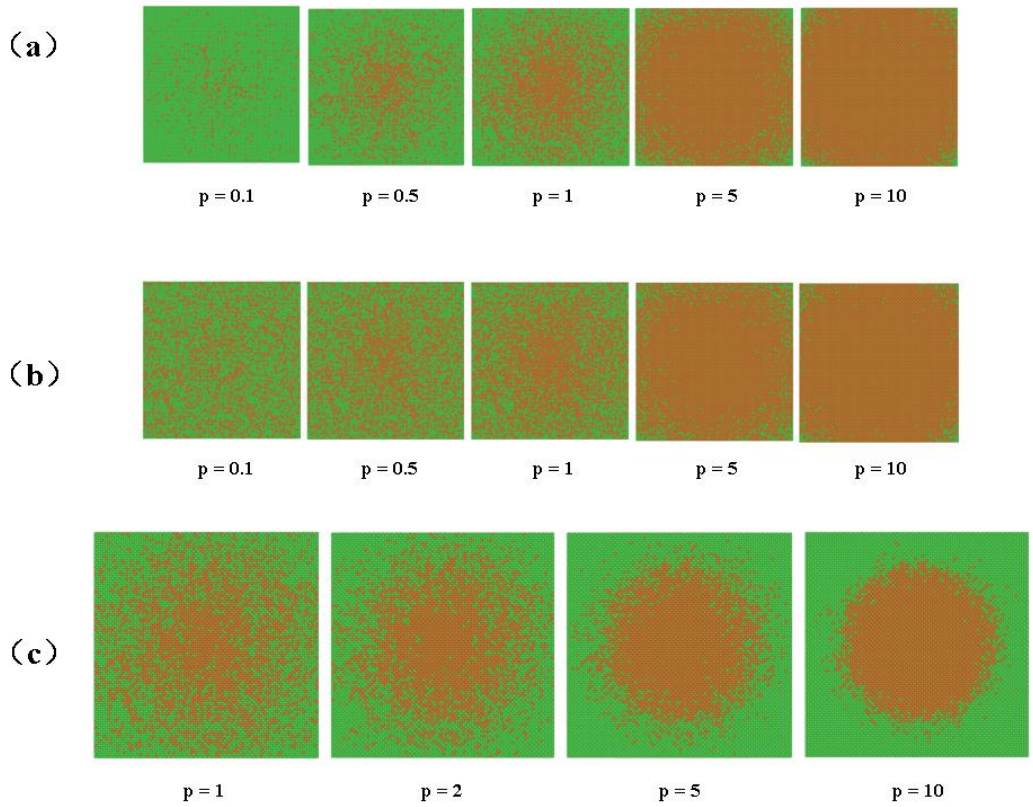


Figure 3: Representative model top view; (a) P-FGM function; (b) E-FGM function; (c) S-FGM function.

3. Analysis of Simulation Results

3.1. Hugoniot validation

In this section, the accuracy of the EAM potential under shock conditions is verified by comparing the shock Hugoniot curves obtained from molecular dynamics simulations with experimental measurements[33][34], as shown in Figure 4. Here, the vertical axis represents pressure, and the horizontal axis, V/V_0, denotes the compression ratio, where V is the initial volume of the sample and V_0 is the volume in the compressed state. The calculated Hugoniot curve for Cu aligns perfectly with the experimental data. For Ni, the simulated Hugoniot curve shows good agreement with the experimental data points when the compression ratio $V/V_0 > 0.75$. However, when $V/V_0 < 0.75$, the simulated pressure results are slightly lower than the experimental values, with a relative error of less than 10%. Therefore, in the molecular dynamics simulations conducted in this study, V/V_0 is maintained within the range greater than 0.75 to ensure that the Hugoniot curves for both Cu and Ni match well with the experimental results.

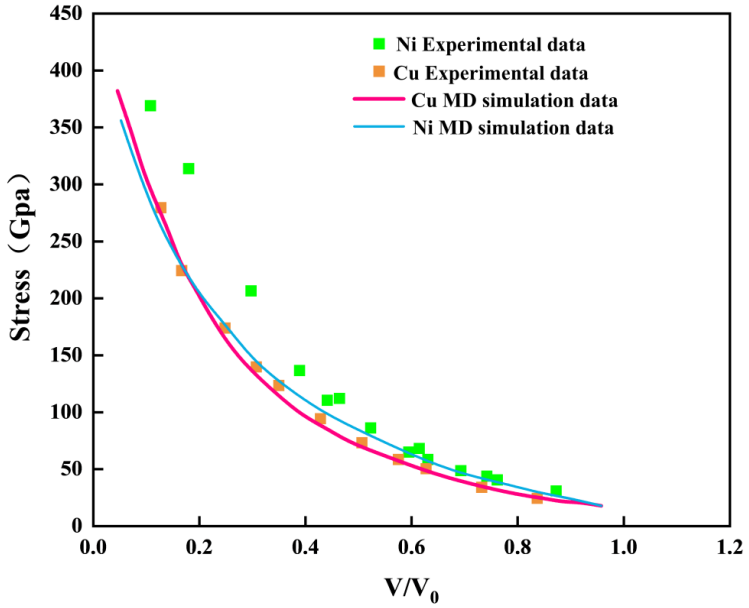


Figure 4: Hugoniot curve validation for Cu-Ni alloy.

3.2. Dynamic evolution of the Cu-Ni FGM model

This section focuses on discussing the dynamic evolution processes of density, temperature, velocity, and stress within the Cu-Ni FGM model. The contour maps for various parameters of the Cu-Ni P-FGM and Cu-Ni S-FGM models under conditions of p = 1 and V = 1.0 km/s are shown in Figures 5, 6, and 7, respectively.

It was found that the trends in the images are consistent when the grading functions are P-FGM, E-FGM, and S-FGM. Therefore, the analysis and discussion primarily focus on the P-FGM function. As shown in Figure 5 (a), the color gradient in the figure clearly reflects the density variation across different regions. In the diagram, the compression zone appears as a high-density region, represented by dark red. During compression, the sample volume decreases compared to its initial state, and the density in the compression zone reaches its maximum value. In the uncompressed zone, the sample density is lower, indicated by a lighter red, reflecting no significant volume change in the sample. The region with the lowest density, i.e., the spallation zone, shows a further decrease in density. This is represented by the blue color band in the figure, illustrating the nucleation and growth processes at multiple locations within this zone. This phenomenon indicates the occurrence of voids and tensile deformation inside the spallation zone, signifying a significant structural change.

As shown in Figure 5 (b), the temperature contour map for p = 1 and V = 1.0 km/s, high-temperature zones are generated in the sample during the spallation stage. The reason for this phenomenon is the generation of a large number of dislocations within the material, which increases the activity of atomic motion. The increase in dislocation density alters the crystal structure, intensifying atomic slip and local plastic deformation, thereby releasing a substantial amount of energy and causing a temperature rise.

Figure5 (c) shows the stress contour map for p = 1 and V = 1.0 km/s, reflecting the mechanical response of the material under instantaneous high-stress loading. Under shock loading conditions, the red band in the figure represents the compression zone. At this stage, the sample is subjected to shock loading, resulting in a region of compressive stress. Combined with Figure 5 (a), this area exhibits the highest density, reflecting the volume reduction and increase in compressive stress during the compression phase. The dark blue band in the figure represents the tensile zone, where the interaction between the release wave and the reflected rarefaction wave leads to the generation of tensile stress. The material undergoes a tensile process under shock loading. The duration of this tensile action is relatively short, making the tensile zone narrower compared to the compression zone. The figure allows for a clear visualization of the different mechanical states of the material during the compression and tensile phases under shock loading.

As shown in Figure 5 (d), the velocity contour map for p = 1 and V = 1.0 km/s is presented. It is evident from the figure that the velocity change at the right end face of the sample is more pronounced. After the compression wave reaches the right end face, the velocity rapidly increases from 1.0 km/s to 2.0 km/s within a short period.

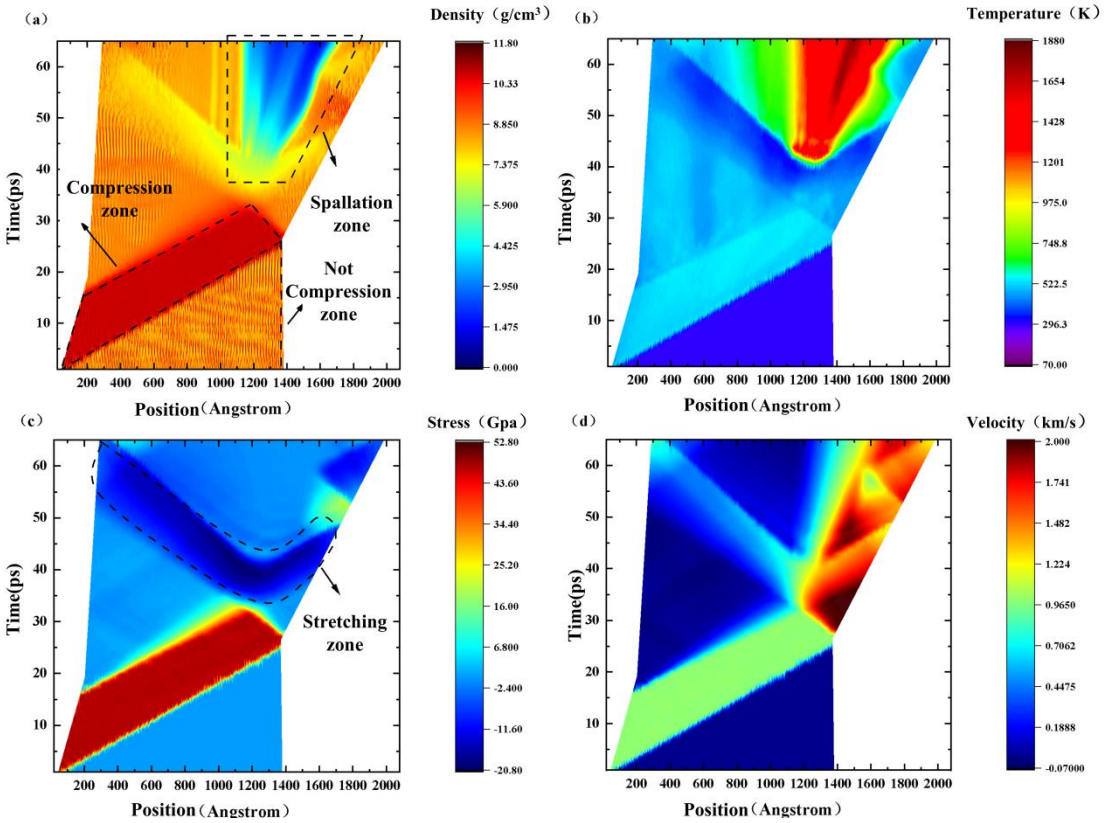


Figure 5 Contour maps of Cu-Ni P-FGM at V = 1.0 km/s, p = 1: (a) Density; (b) Temperature; (c) Stress; (d) Velocity.

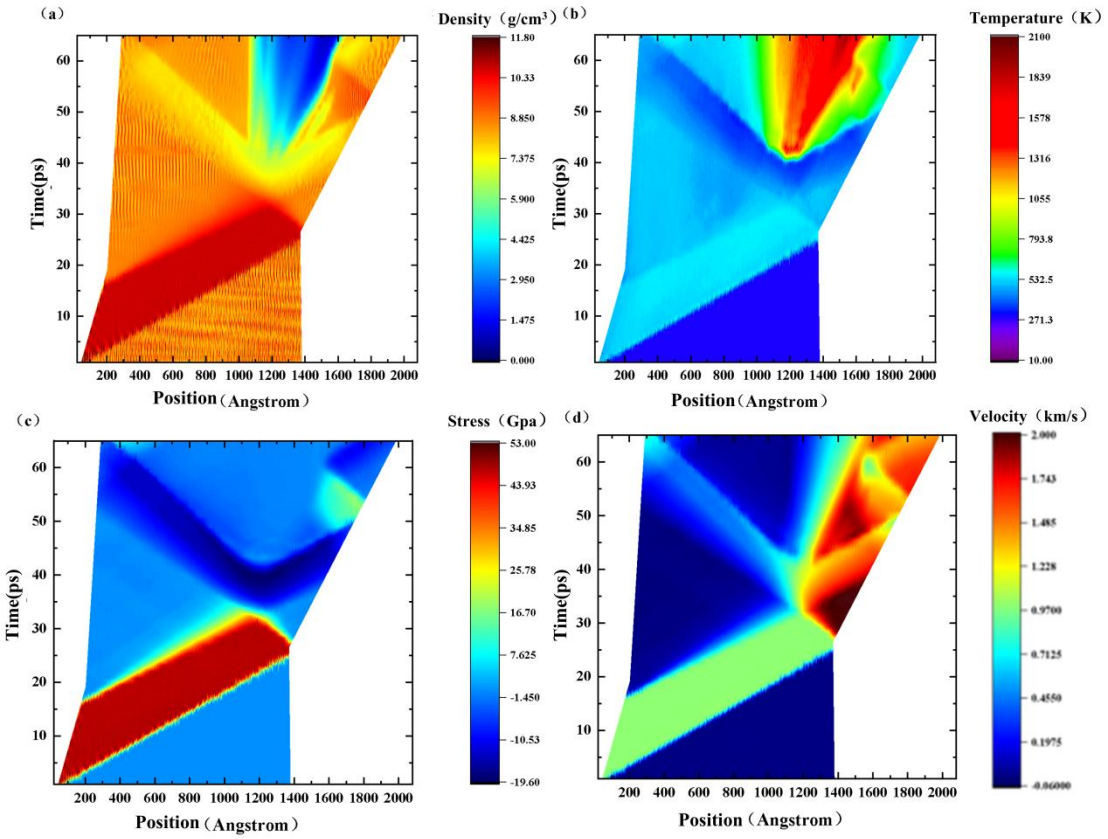


Figure 6 Contour maps of Cu-Ni E-FGM at V = 1.0 km/s, p = 1: (a) Density; (b) Temperature; (c) Stress; (d) Velocity.

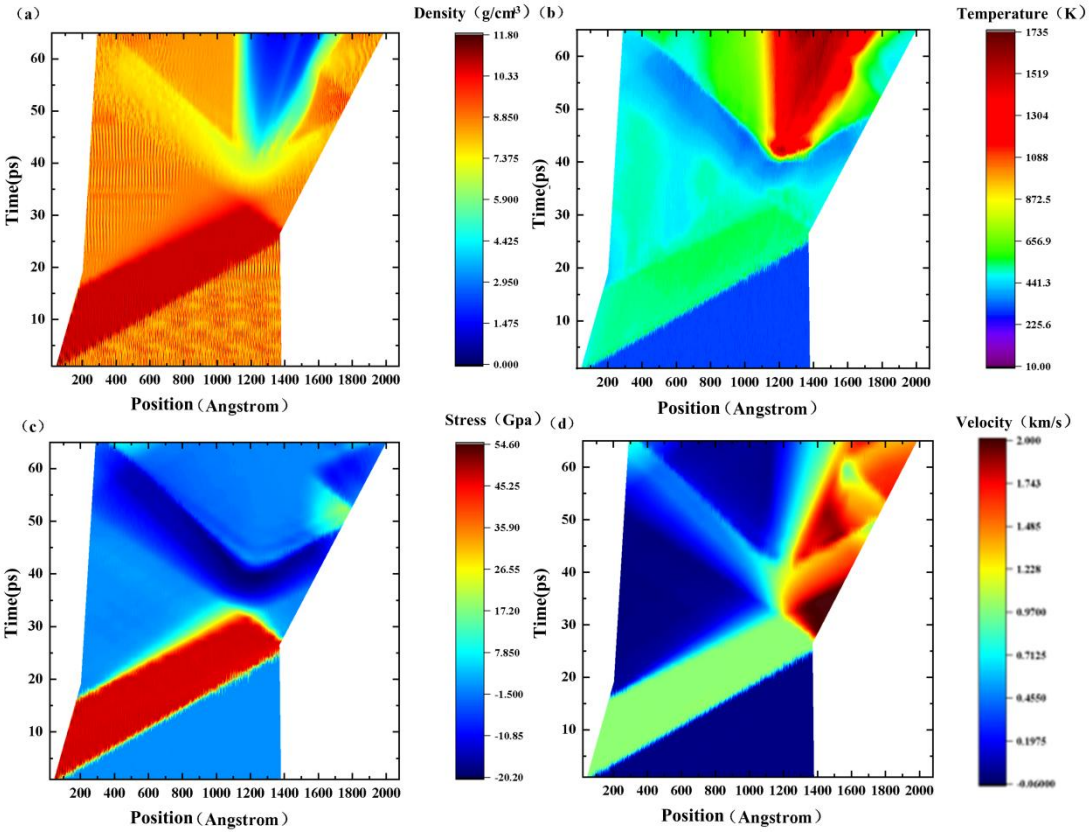


Figure 7 Contour maps of Cu-Ni S-FGM at V = 1.0 km/s, p = 1: (a) Density; (b) Temperature; (c) Stress; (d) Velocity.

As shown in Figure 8, to observe the dynamic evolution process of the elastoplastic deformation in the Cu-Ni P-FGM sample more clearly, a 50 Å region extending symmetrically from the center point along the x-direction was selected for analysis and designated as slice S.

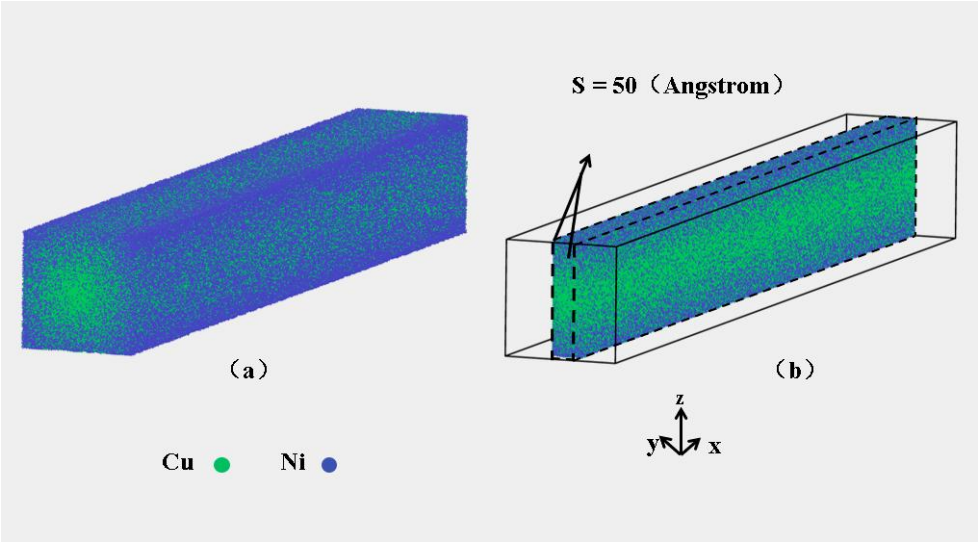


Figure 8 (a) Overall structure of the Cu-Ni P-FGM sample; (b) A 50 Å thick sample section extracted along the x-direction at the center point.

As shown in Figure 9 (a), it depicts the atomic configuration of the Cu-Ni P-FGM sample. When p = 1, the total length of the model is 1437.53 Å. As the simulation proceeds, the sample undergoes multiple stages of loading and deformation. At t = 16.25 ps, the "reflective wall" of the sample separates, marking the generation of the release rarefaction wave. The compression wave propagates to the midpoint of the sample, at which point the sample length reaches its minimum state throughout the simulation. At t = 38.75 ps, as shown in Figure 9 (c), the sample enters the tensile stage. The tensile stress causes the sample length to exhibit a recovery trend, gradually increasing. Subsequently, the sample enters the spallation stage. In Figure 9 (e), at t = 38 ps, the white areas in the figure represent the nucleation sites of voids, which are relatively small in volume at this time. As time progresses, the number of nucleation sites gradually increases, and during the initial stage of spallation, the number of nucleation sites continues to rise, as shown in Figure9 (f). In this stage, the sample begins to elongate under tensile stress, displaying the deformation process of the sample under tension and the void nucleation process. In Figures 9 (e) to (h), the growth and coalescence of voids can be observed. From t = 48 ps to t = 52 ps, the pores marked by dashed lines gradually merge, eventually forming a larger pore. This period indicates further damage and failure of the sample under tensile stress. As damage accumulates, the failure of the sample becomes more pronounced, with crack and pore coalescence promoting the overall failure of the sample. By the end of the simulation at t = 65 ps, after undergoing tensile and spallation processes, the total length of the sample increases to 1930 Å, and obvious deformation and damage can be seen in the atomic configuration. Under shock loading, the Cu-Ni P-FGM undergoes multiple stages, including compression, tension, spallation, and pore coalescence, ultimately leading to material deformation and damage. The damage mechanism is primarily characterized by the nucleation, growth, and aggregation of voids.

During the spallation process of the sample, the temperature around the voids rises rapidly after void nucleation begins. At t = 38.75 ps, when void nucleation just initiates, most of the sample remains at a low temperature. However, the temperature around the voids increases significantly, exceeding the melting point of the sample, indicating that the material around the voids is in a locally molten state. When t = 40 ps, the voids begin to grow. At this time, the temperature distribution in the sample remains uneven, with areas farther from the voids being colder than those near the voids.

As the voids continue to grow and coalesce, the area of the high-temperature region expands, and the average temperature around the voids in the sample gradually increases. During the spallation cavitation process, the temperature rise is mainly caused by plastic heat dissipation. At this stage, the sample remains solid during the shock compression and release phases. The processes of void nucleation, growth, and coalescence are accompanied by plastic deformation of the solid material. The work of plastic deformation is largely converted into heat, causing the temperature around the voids to rise continuously. On the other hand, the increase in temperature reduces the viscosity and strength of the material, especially as the temperature approaches the melting point, leading to a rapid decline in material strength. The reduction in material strength and viscosity promotes the growth and coalescence of voids. In summary, heat dissipation and the processes of void nucleation, growth, and coalescence mutually reinforce each other.

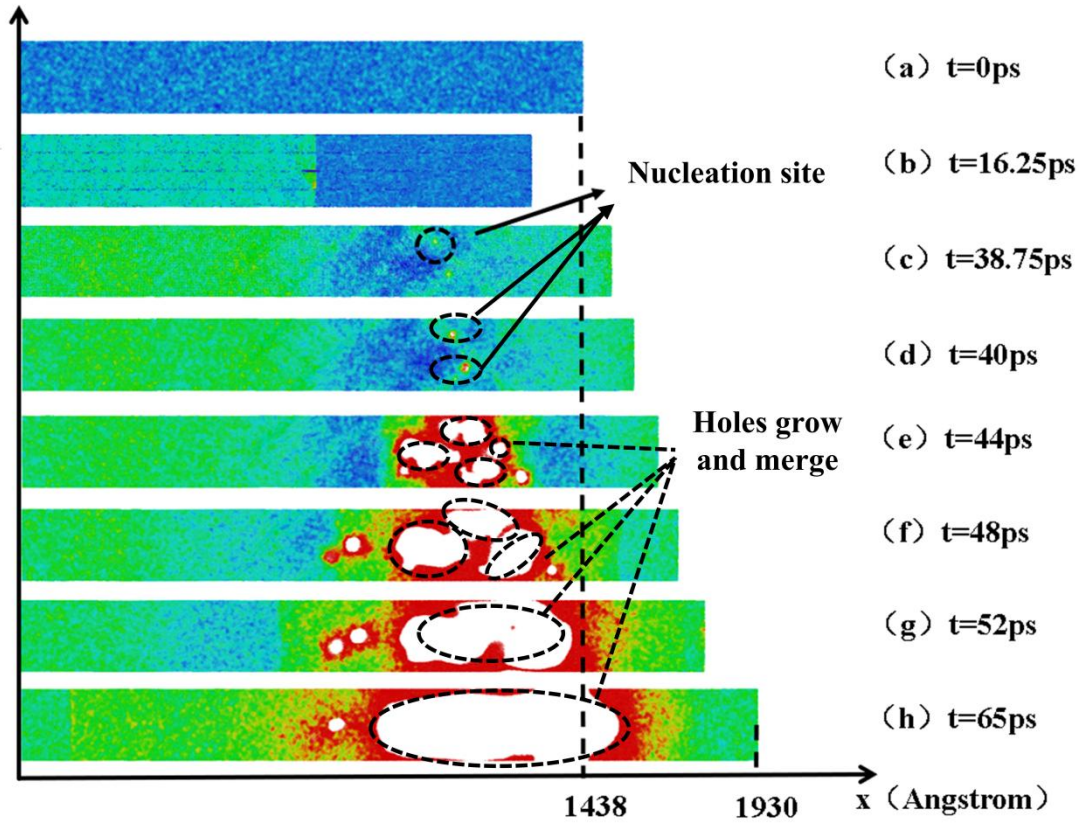


Figure 9 Schematic diagram of atomic temperature distribution in Cu-Ni P-FGM at different time instances during the evolution process.

3.3. Effect of function parameter p on the Cu-Ni FGM NWs model

As shown in Figure10, the changes in the number of voids in the samples under impact loading for the Cu-Ni P-FGM, E-FGM, and S-FGM models with different p values are presented. As illustrated, during impact loading, the evolution of voids undergoes several stages over time. As seen in Figures10 (a) and (b), the first stage is void nucleation, where stress concentration within the material triggers the initial formation of voids. The second stage sees a significant increase in the number of voids as tension continues. Finally, the process enters the void coalescence stage, where multiple small voids gradually merge to form larger ones.

With an increase in the p value (the proportion of copper in the sample), it can be observed that the maximum number of voids during the spallation process increases significantly. The primary reason for this is that copper has a lower melting point (1085°C) compared to nickel (1455°C). As the copper content increases, the alloy's melting point decreases, making the material more susceptible to local softening, thermal stress concentration, and grain boundary weakening under impact loading. This facilitates easier nucleation and growth of voids within the material, leading to an increase in their number. Thus, the increase in copper content significantly influences the damage behavior of the material under impact loading by affecting the alloy's melting point and thermophysical properties.

The trend in the number of voids for the Cu-Ni S-FGM model is consistent with that of the Cu-Ni P-FGM and Cu-Ni E-FGM models. However, as shown in Figure 10(c), in the Cu-Ni S-FGM model, when the distribution of Cu atoms is more concentrated at the center of the sample, the maximum number of voids during the spallation process increases.

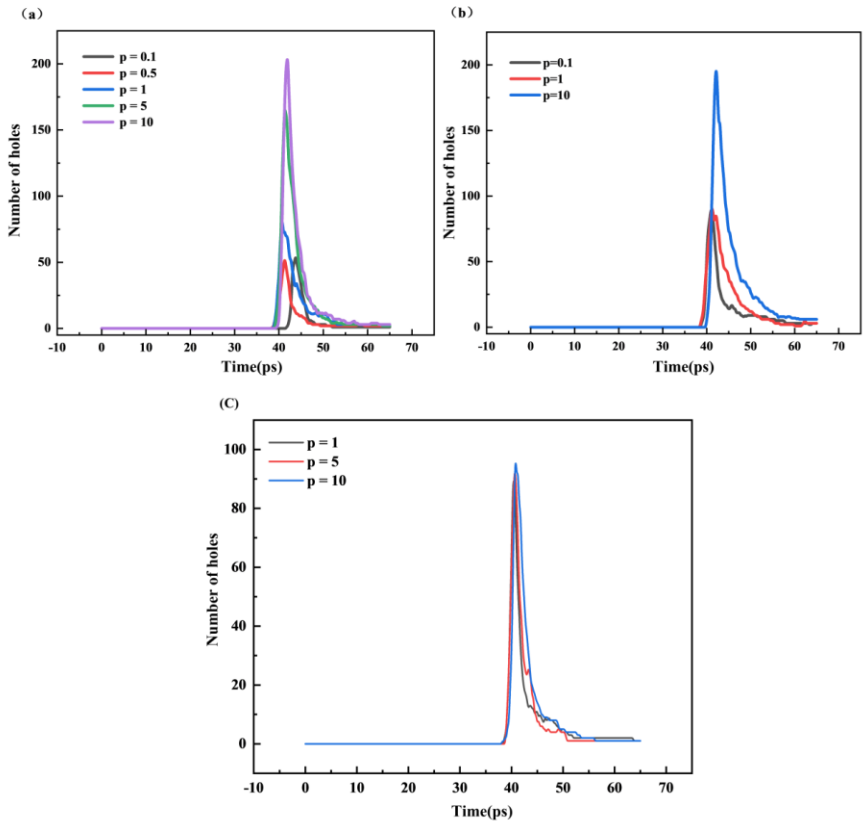


Figure 10 Number of voids changes in the Cu-Ni FGM model under impact loading with different p-values: (a) Cu-Ni P-FGM model; (b) Cu-Ni E-FGM model; (c) Cu-Ni S-FGM model.

To investigate the influence of the function parameter *p* on the damage and failure of Cu-Ni P-FGM, the free surface velocity profiles for different *p* values were plotted, as shown in Figure 11, and the spall strength of the samples was calculated. Under the same impact velocity, different function parameters *p* result in slight variations in the peak values of the free surface velocity profiles and differences in the oscillation amplitudes. These differences directly lead to changes in the pullback velocity Δu, which in turn affects the material's spall strength. When p = 0.1, Δu is the largest among the three curves; when p = 10, Δu is the smallest among the three *p* values. Furthermore, the spall strength (σsp) is defined as the maximum tensile stress during the spallation process. In molecular dynamics simulations, performing a binning analysis allows for convenient measurement of the maximum stress in the sample at each timestep. The maximum stress of the sample can then be identified at the initial timestep of spallation.

$$\sigma_{sp} = \max_{X,t} \sigma(X,t) \tag{2}$$

In the formula: $\sigma(X,t)$ is the stress in the material at point X at time t.

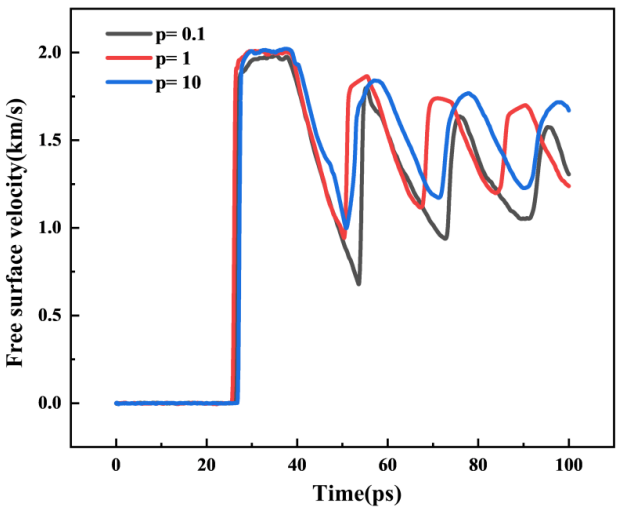


Figure 11: Free surface velocity history of Cu-Ni P-FGM under different function parameters p, V = 1.0 km/s.

Table 3 and Figure12 present the influence of the function parameter p on the spall strength of P-FGM and E-FGM models at V = 1.0 km/s. For the radially graded Cu-Ni P-FGM and E-FGM functionally graded materials with a power-law distribution, the function parameter $p$has a significant impact on the spall strength. As the p value increases, the spall strength of the Cu-Ni P-FGM and E-FGM models gradually decreases. This trend arises from the interaction between the change in atomic composition and abrupt changes at the alloy interface. On one hand, as the parameter p increases, the proportion of Ni atoms in the Cu-Ni P-FGM and E-FGM models decreases while the proportion of Cu atoms increases. Since single-crystal Ni has higher strength than single-crystal Cu, the spall strength decreases. On the other hand, the Cu-Ni alloy at the interface where composition changes abruptly experiences stress concentration, which affects the mechanical properties of the material. The interaction of these two effects ultimately leads to a reduction in spall strength as the function parameter p increases.

For the Cu-Ni S-FGM with a sigmoid function distribution, the spall strength of the model also gradually decreases as the p value increases. In this process, the structural distribution of Cu atoms becomes the dominant factor influencing the spall strength of the sample.

Table 3 Effect of function parameter p on the spall strength of Cu-Ni P-FGM.

Types of FGM	V	p	Spall strength(σ_{sp})
P-FGM	1.0 km/s	0.1	22.18 Gpa
		0.5	21.72 Gpa
		1	20.50 Gpa
		5	19.43 Gpa
		10	18.89 Gpa
E-FGM	1.0 km/s	0.1	20.22 Gpa
		1	19.29 Gpa
		10	18.11 Gpa
S-FGM	1.0 km/s	1	20.11 Gpa
		5	18.93Gpa
		10	18.74Gpa

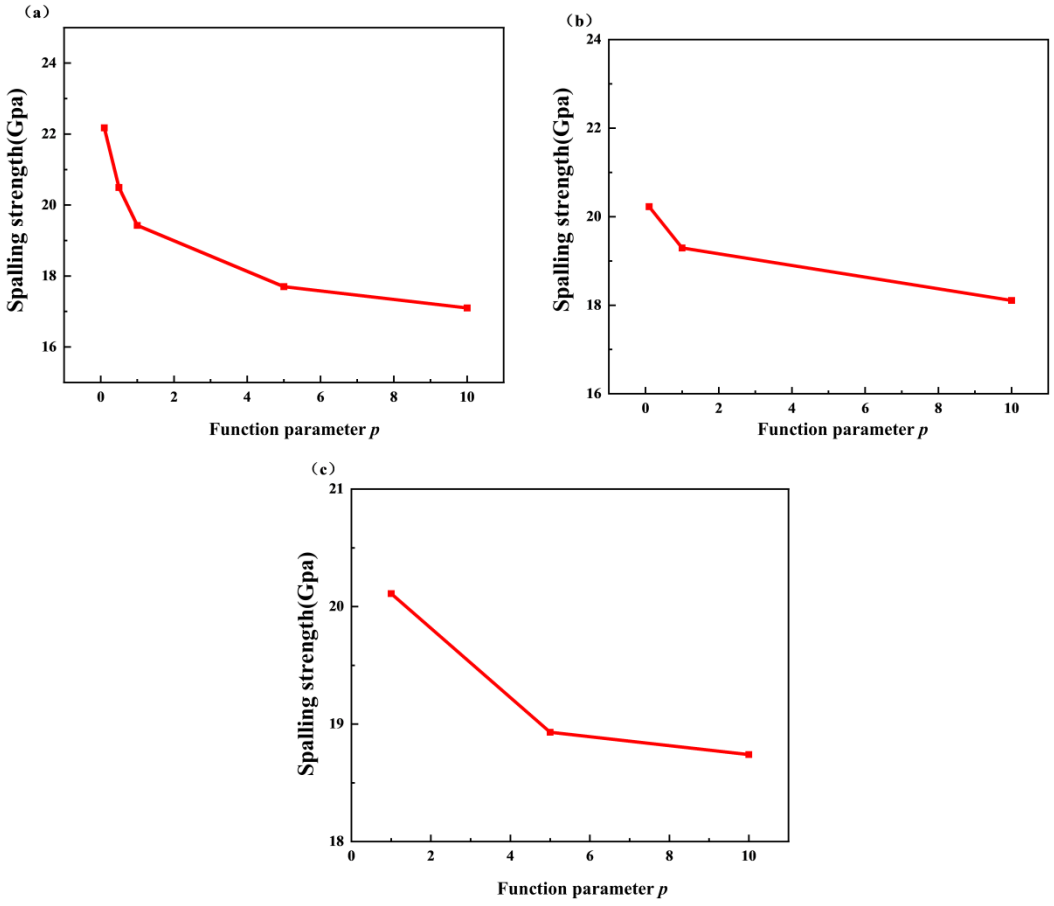


Figure 12 Spall strength of the Cu-Ni FGM model under different function parameters p: (a) Cu-Ni P-FGM model; (b) Cu-Ni E-FGM model; (c) Cu-Ni S-FGM model.

4. Conclusion

(1) The simulation results of the Cu-Ni functionally graded material with a power-law radial distribution were compared with the Hugoniot curves. When $V/V_0 > 0.75$, the results show a high agreement with the experimental data. By comparing the calculated impact pressure with the experimental pressure, the reliability of the potential function was verified. This demonstrates the reliability of the simulation method, providing a solid foundation for the subsequent study of dynamic damage in spallation and microspallation.

(2) Using an atomic-scale modeling approach, Cu-Ni FGM NWs were generated, and the mechanical responses of Cu-Ni alloy functionally graded models with different radial

gradients—power-law (P-FGM), exponential (E-FGM), and sigmoid (S-FGM) functions—were analyzed. The waveform structures of the Cu-Ni alloy under impact loading, the dynamic evolution of the Cu-Ni FGM NWs model, and variations in key parameters such as density, temperature, free-surface velocity, spall strength, and void number with changes in the grading function, the functional variable p in detail.

(3) In studying the dynamic evolution of the Cu-Ni FGM NWs model, the trends in the dynamic evolution processes of density, temperature, velocity, and stress were consistent for the three functions: P-FGM, E-FGM, and S-FGM. Throughout the impact loading process, the sample undergoes a compression phase, generating strain, followed by a tensile phase where deformation gradually recovers, and finally, tensile stress leads the sample into the spallation phase, characterized by void growth, nucleation, and coalescence. In investigating the effect of the function parameter p on the model, for the P-FGM and E-FGM functions, an increase in the p-value (the proportion of copper in the sample) results in the formation of a denser compression zone in the high-copper alloy under shock loading, leading to an increase in the number of voids, a decrease in spall strength, and a reduction in the free-surface velocity profile. In the S-FGM function, as the p-value increases (copper atoms become more concentrated at the sample center, while the overall proportion of copper slightly decreases), the model exhibits higher density in the compression region under impact loading, an increase in the number of voids, and a lower spall velocity. In this case, the distribution of Cu atoms plays the dominant role in influencing the sample's behavior.

(4) During the processes of void nucleation, growth, and coalescence, on one hand, the work of plastic deformation is largely converted into thermal energy, causing the temperature around the voids to continuously rise. On the other hand, the increase in temperature reduces the viscosity and strength of the material, leading to a rapid decline in material strength. The reduction in material strength and viscosity further promotes the growth and coalescence of voids.

Reference

[1] Shanmugavel P, Bhaskar G B, Chandrasekaran M, et al. An overview of fracture analysis in functionally graded materials[J]. European Journal of Scientific Research, 2012, 68(3): 412-439.

[2] Wang S S. Fracture mechanics for delamination problems in composite materials[J]. Journal of composite materials, 1983, 17(3): 210-223.

[3] Mueller E, Drašar Č, Schilz J, et al. Functionally graded materials for sensor and energy applications[J]. Materials Science and Engineering: A, 2003, 362(1-2): 17-39.

[4] Kaysser W, Bartsch M, Peters M, et al. Functional gradients for novel microstructures[J]. Adv. Sci. Technol. 31, 2002: 341-353.

[5] Noda N. Thermal stresses in functionally graded materials[J]. Journal of Thermal Stresses, 1999, 22(4-5): 477-512.

[6] Chen P Y, McKittrick J, Meyers M A. Biological materials: functional adaptations and bioinspired designs[J]. Progress in Materials Science, 2012, 57(8): 1492-1704.

[7] Studart A R. Biological and bioinspired composites with spatially tunable heterogeneous architectures[J]. Advanced Functional Materials, 2013, 23(36): 4423-4436.

[8] Studart A R. Additive manufacturing of biologically-inspired materials[J]. Chemical Society Reviews, 2016, 45(2): 359-376.

[9] Yoo D J. New paradigms in cellular material design and fabrication[J]. International Journal of Precision Engineering and Manufacturing, 2015, 16(12): 2577-2589.

[10] Yoo D J. Recent trends and challenges in computer-aided design of additive manufacturing-based biomimetic scaffolds and bioartificial organs[J]. International journal of precision engineering and manufacturing, 2014, 15(10): 2205-2217.

[11] Chen F, Jia M, She Y, et al. Mechanical behavior of AlN/Mo functionally graded materials with various compositional structures[J]. Journal of Alloys and Compounds, 2020, 816: 152512.

[12] Wagih A, Attia M A, AbdelRahman A A, et al. On the indentation of elastoplastic functionally graded materials[J]. Mechanics of Materials, 2019, 129: 169-188.

[13] Gerk C, Willert-Porada M. Development of graded composite electrodes for the SOFC[C]//Materials science forum. Trans Tech Publications Ltd, 1999, 308: 806-813.

[14] Jedamzik R, Neubrand A, Rödel J. Characterisation of electrochemically processed graded tungsten/copper composites[C]//Materials science forum. Trans Tech Publications Ltd, 1999, 308: 782-787.

[15] Ma S, Xue D, Li Q, et al. Stress analysis of solid oxide fuel cell electrodes using functional gradient materials[J]. Journal of The Electrochemical Society, 2023, 170(3): 034502.

[16] Boggarapu V, Sreekanth P S R, Peddakondigalla V B. Microstructure, mechanical and tribological properties of Al/Cu functionally graded material fabricated through powder metallurgy[J]. Journal of Engineering Research, 2024, 12(3): 502-510.

[17] Liao Y, Li P, Jia J, et al. Molecular dynamics simulation of Au-Ag nanowires under tensile loading[J]. Computational materials science, 2023, 220: 112043.

[18] Zhou A, Liu X B, Wang Q, et al. Investigation of nano-tribological behaviors and deformation mechanisms of Cu-Ni alloy by molecular dynamics simulation[J]. Tribology International, 2023, 180: 108258.

[19] Fang T H, Wu C D, Chang W J. Molecular dynamics analysis of nanoimprinted Cu–Ni alloys[J]. Applied surface science, 2007, 253(16): 6963-6968.

[20] Moita J S, Araújo A L, Correia V F, et al. Material distribution and sizing optimization of functionally graded plate-shell structures[J]. Composites Part B: Engineering, 2018, 142: 263-272.

[21] Moleiro F, Correia V M F, Araújo A L, et al. Deformations and stresses of multilayered plates with embedded functionally graded material layers using a layerwise mixed model[J]. Composites part B: engineering, 2019, 156: 274-291.

[22] Song M, Yang J, Kitipornchai S. Bending and buckling analyses of functionally graded polymer composite plates reinforced with graphene nanoplatelets[J]. Composites Part B: Engineering, 2018, 134: 106-113.

[23] Zaoui F Z, Ouinas D, Tounsi A. New 2D and quasi-3D shear deformation theories for free vibration of functionally graded plates on elastic foundations[J]. Composites Part B: Engineering, 2019, 159: 231-247.

[24] Woo J, Meguid S A. Nonlinear analysis of functionally graded plates and shallow shells[J]. International Journal of Solids and structures, 2001, 38(42-43): 7409-7421.

[25] Sachdeva C, Padhee S S. Functionally graded cylinders: Asymptotically exact analytical formulations[J]. Applied Mathematical Modelling, 2018, 54: 782-802.

[26] Praveen G N, Reddy J N. Nonlinear transient thermoelastic analysis of functionally graded ceramic-metal plates[J]. International journal of solids and structures, 1998, 35(33): 4457-4476.

[27] Shishesaz M, Hosseini M. Mechanical behavior of functionally graded nano-cylinders under radial pressure based on strain gradient theory[J]. Journal of Mechanics, 2019, 35(4): 441-454.

[28] Zhao Y, Zhang Y, Li Y, et al. Rapid and large-scale synthesis of Cu nanowires via a continuous flow solvothermal process and its application in dye-sensitized solar cells (DSSCs)[J]. RSC advances, 2012, 2(30): 11544-11551.

[29] Foiles S M, Baskes M I, Daw M S. Embedded-atom-method functions for the fcc metals Cu, Ag, Au, Ni, Pd, Pt, and their alloys[J]. Physical review B, 1986, 33(12): 7983.

[30] Bonny G, Pasianot R C, Malerba L. Fitting interatomic potentials consistent with

[31] hermodynamics: Fe, Cu, Niandtheir alloys[J]. Philosophical Magazine, 2009, 89(34-36):

[32] Jin Z H, Paulino G H. Transient thermal stress analysis of an edge crack in a functionally graded material[J]. International Journal of Fracture, 2001, 107(1): 73-98.

[33] Jin Z H, Batra R C. Stress intensity relaxation at the tip of an edge crack in a functionally graded material subjected to a thermal shock[J]. Journal of thermal stresses, 1996, 19(4): 317-339.

[34] Jin Z H, Batra R C. Stress intensity relaxation at the tip of an edge crack in a functionally graded material subjected to a thermal shock[J]. Journal of thermal stresses, 1996, 19(4): 317-339

[35] Demaske B J, Zhakhovsky V V, White C T, et al. A new nickel EAM potential for atomistic simulations of ablation, spallation, and shockwave phenomena[C]//AIP Conference Proceedings. American Institute of Physics, 2012, 1426(1): 1211-1214.

[36] Marsh S P. LASL shock Hugoniot data[M]. University of California Press, 1980.